Figure S1. Datasets overview.

		Mouse						
	Age	1m	3m	7m	18m	21m	24m	30m
	Aorta	√	√		√	√	√	√
	BAT		√		√		√	
	Bladder	√	√		√		√	
	Brain (Myeloid)		√	√	√		√	
	Brain (Non-Myeloid)		√	√	√		√	
	Diaphragm		√		√		√	
	Fat				√	√		√
	GAT		√		√		√	
	Heart	√	√		√	√	√	√
	Kidney		√		√	√	√	√
	Large Intestine		√		√		√	√
	Limb Muscle	√	√		√	√	√	√
	Liver	√	√		√	√	√	√
	Lung	√	√		√	√	√	√
	Mammary Gland		√		√	√		
	Marrow	√	√		√	√	√	√
	MAT		√		√		√	
	Pancreas		√		√	√	√	√
	SCAT		√		√		√	
	Skin		√		√	√	√	
	Spleen	√	√		√	√	√	√
	Thymus		√		√	√	√	
	Tongue	√	√		√		√	
	Trachea		√		√		√	
	WAT							

Figure S1. Dataset overview.

Figure S2. Standard Elastic Net model is less robust and less accurate.

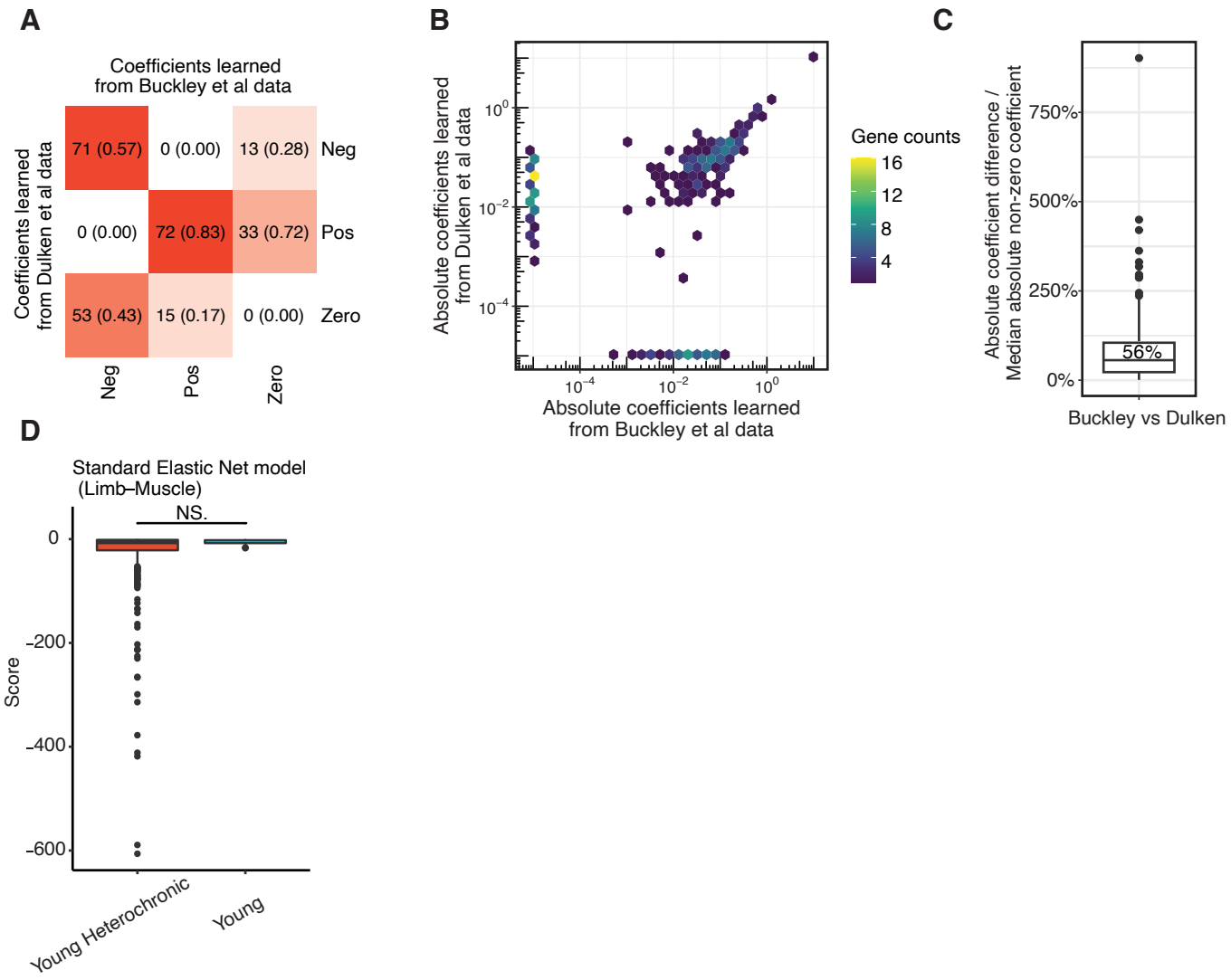

Figure S2. Standard Elastic Net model is less robust and less accurate.
(A-C) Difference in coefficients of standard Elastic Net models trained on two different brain scRNA-seq datasets (Dulken et al. 2019; Buckley et al. 2023). We kept genes that have non-zero coefficients in at least one model for comparison. (A) Changes in coefficient sign. For example, 53 (43%) genes with a negative coefficient when trained on the Buckley et al data have a zero coefficient when trained on the Dulken et al data. (B) Scatter plot of absolute coefficients of each gene learned in the two datasets. Horizontal and vertical lines (x = 1e-5, y = 1e-5) represents genes with zero coefficients in one model (1e-5 is the pseudo-value added to coefficients before log transform). (C) Boxplot of absolute coefficient differences between two models. To calculate relative changes (y-axis), we divided the absolute difference against the median absolute coefficient across models among all genes (0.05786675). Data showed that the median absolute coefficient difference is around 56% of the median absolute coefficient value.
(D) Aging scores of limb muscle cells from young mice and young heterochronic mice calculated by standard Elastic Net model trained on limb muscle cells of different chronological ages. ***p-value < 0.001 using a two-sided unpaired Student's *t*-test.

Figure S3. Breakdown of Aging Map collections.

A

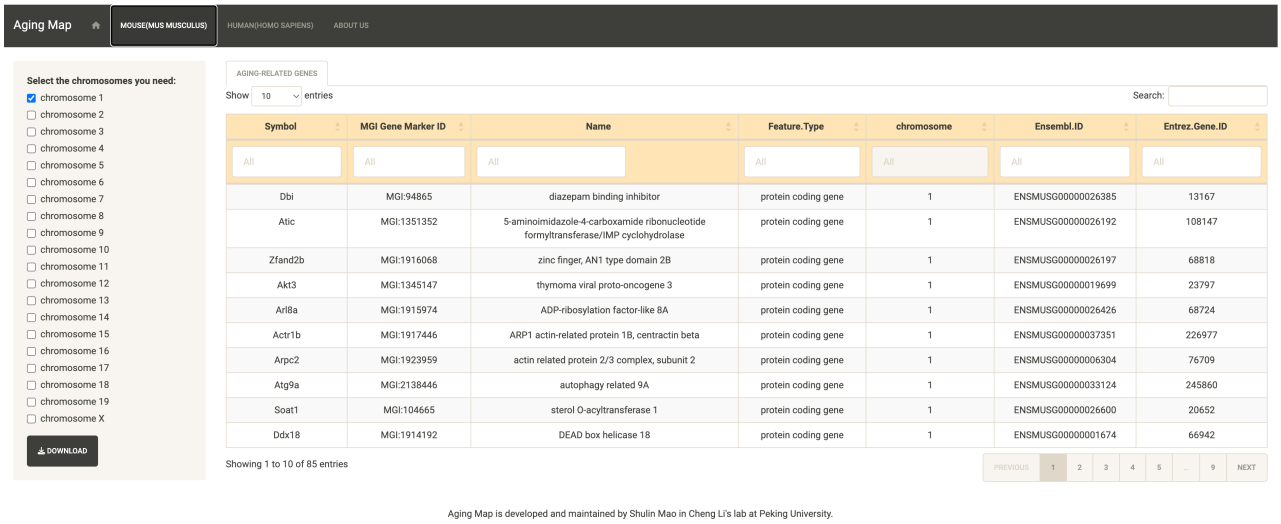

B

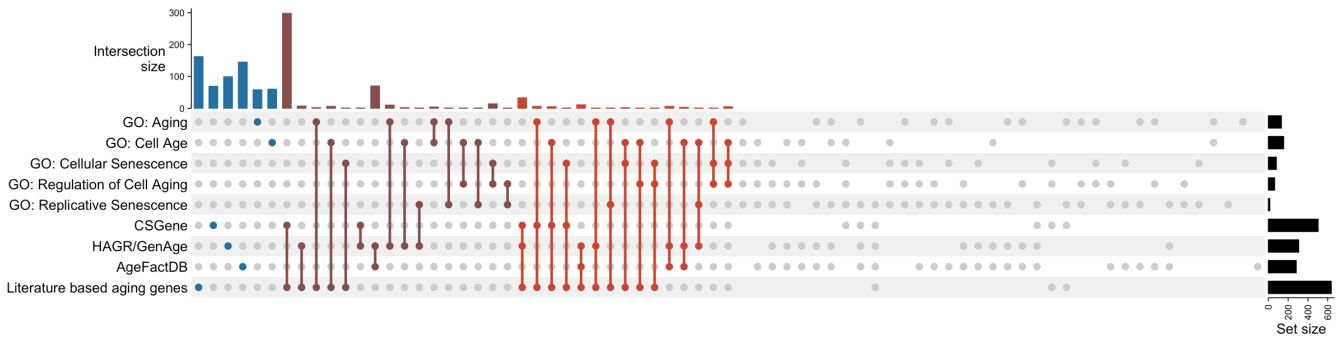

C

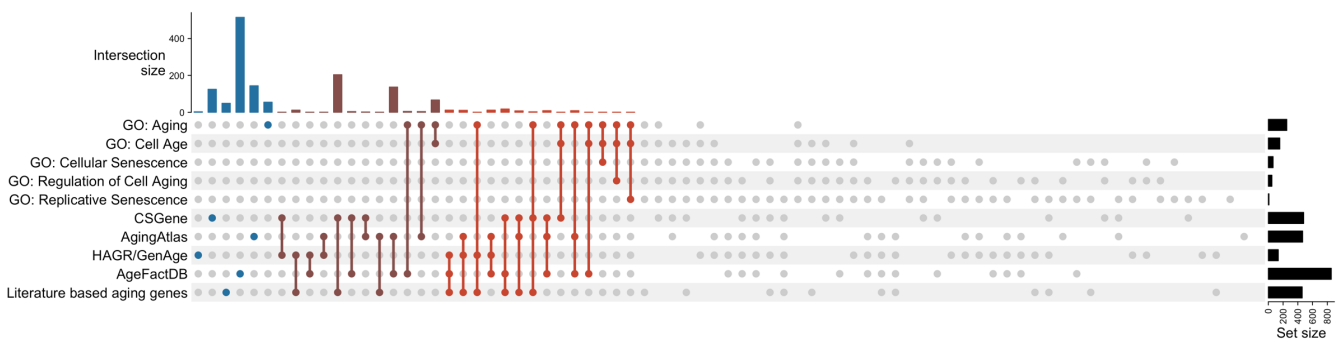

D

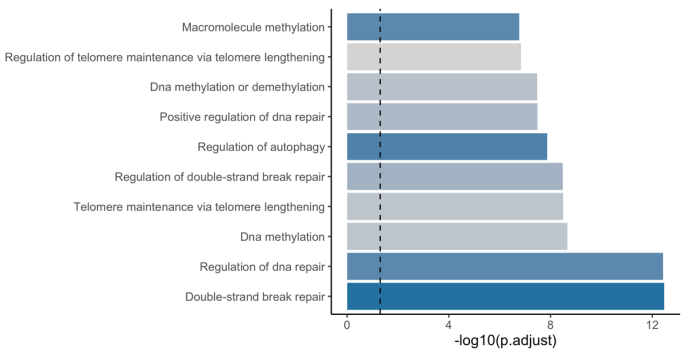

E

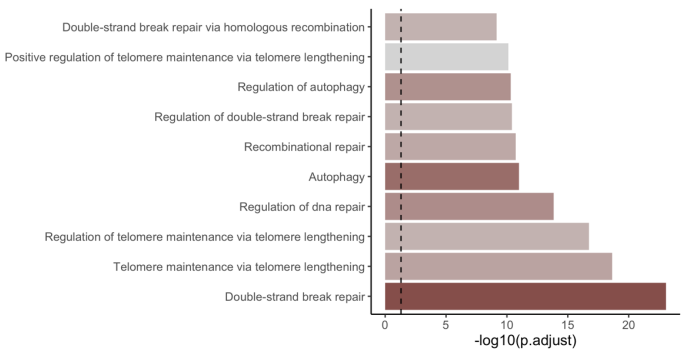

Figure S3. Breakdown of Aging Map collections.
(A) The Aging Map web interface.
(B and C) Upset plots showing the overlap of human (B) and mouse (C) aging genes from different sources. Combination sets (columns) are mutually exclusive. For example, the first column in B represents human genes that are only covered by the PubMed text-mining list.
(D and E) Similar to Figure 2C and D but showing the enrichments of known aging GO terms (DNA repair, methylation, Telomere length and autophagy) in human (D) and mouse (E) literature-confirmed aging genes.

Figure S4. Global Gene Expression measure in different tissues

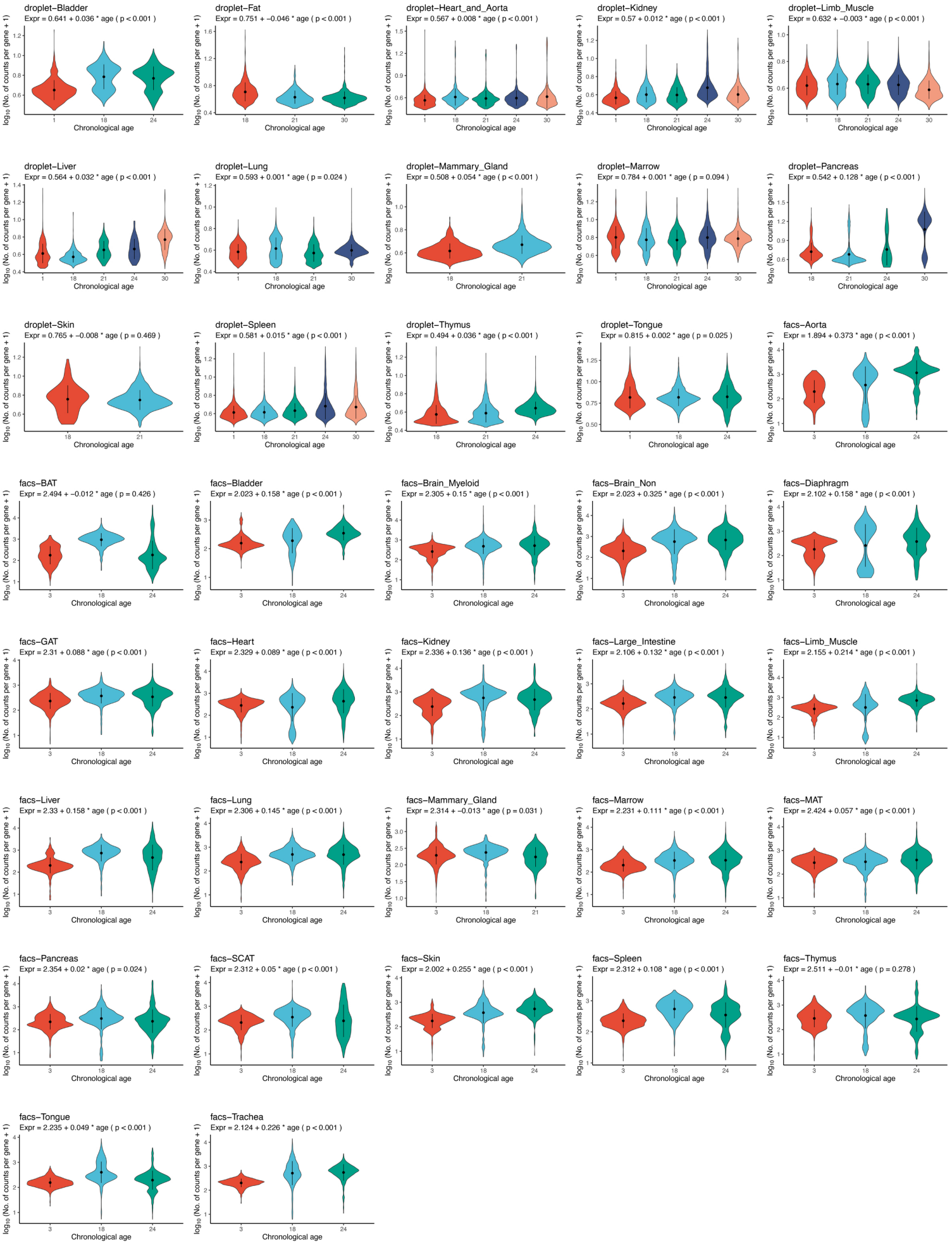

Figure S4. Global Gene Expression of cells in different tissues.
Violin plots showing the distributions of "Global Gene Expression" defined as log-transformed mean counts per gene of cells in different tissues and different chronological age groups. For each tissue we fitted a linear regression model as reported in the figure.

Figure S5. Single-cell Entropy of cells in different tissues.

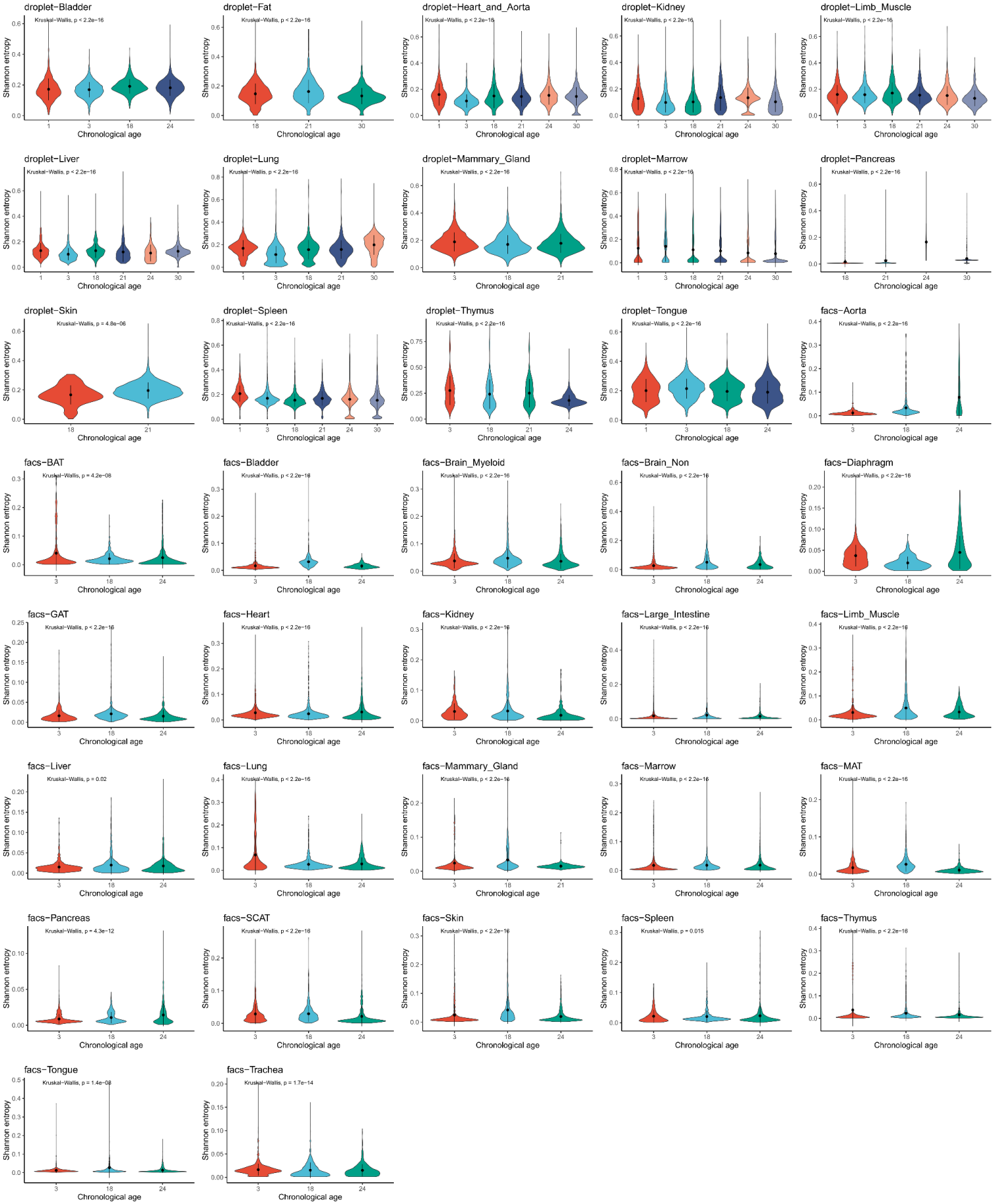

Figure S5. Single-cell Entropy of cells in each sample.
Similar to Figure. S4 except showing distributions of "Single-cell Entropy". See Methods for detailed definition. p-values were calculated using the Kruskal-Wallis test.

Figure S6. Overview of the Elastic Net-based forward selection method

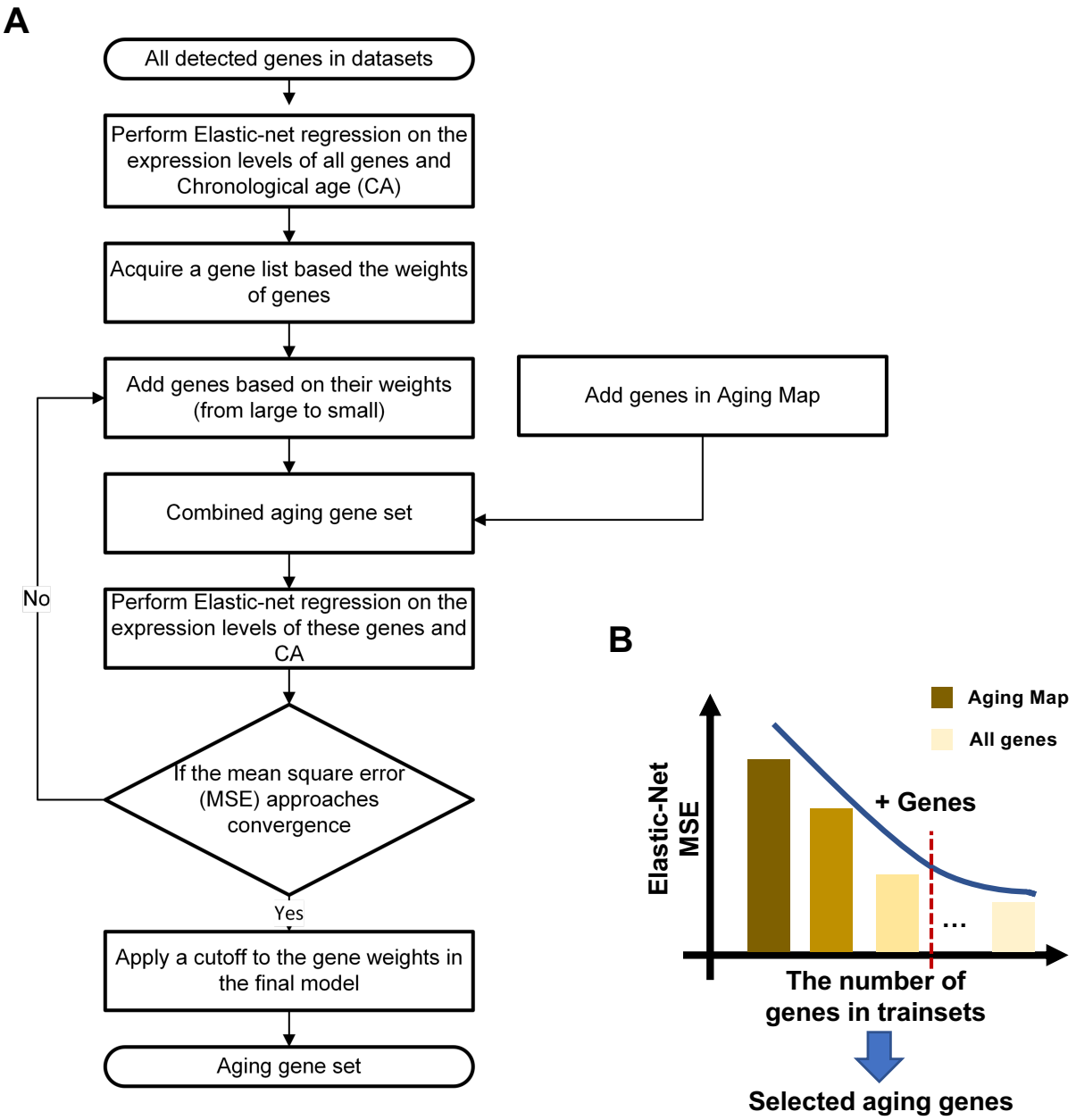

Figure S6. Overview of the Elastic Net-based forward selection method.
(A) Flow chart showing the selection process of tissue-specific aging genes
(B) Demonstration of the stop criterion. The red dotted line shows the cut off position.

Figure S7. Training SCALE

A

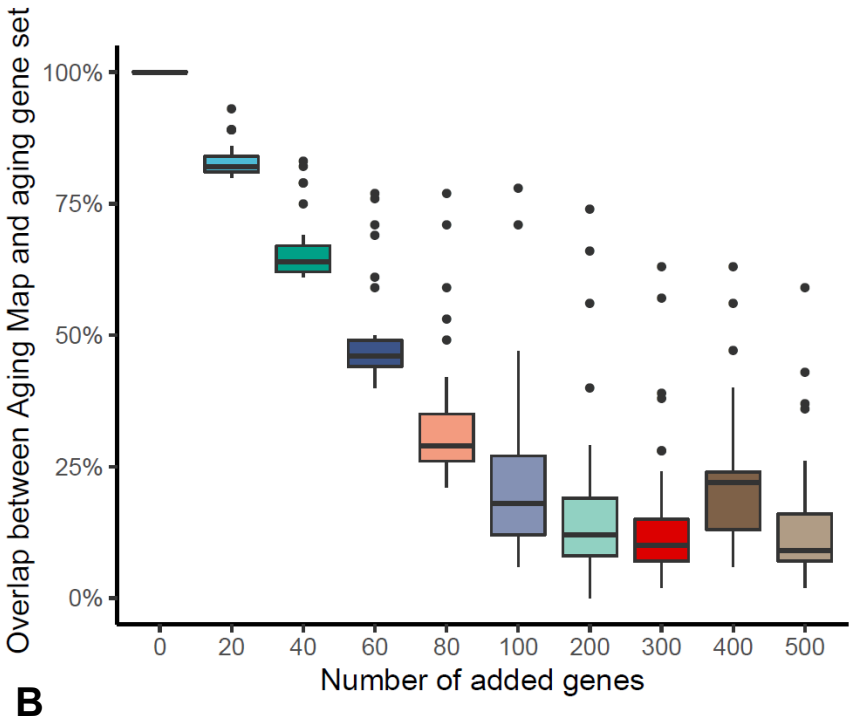

B

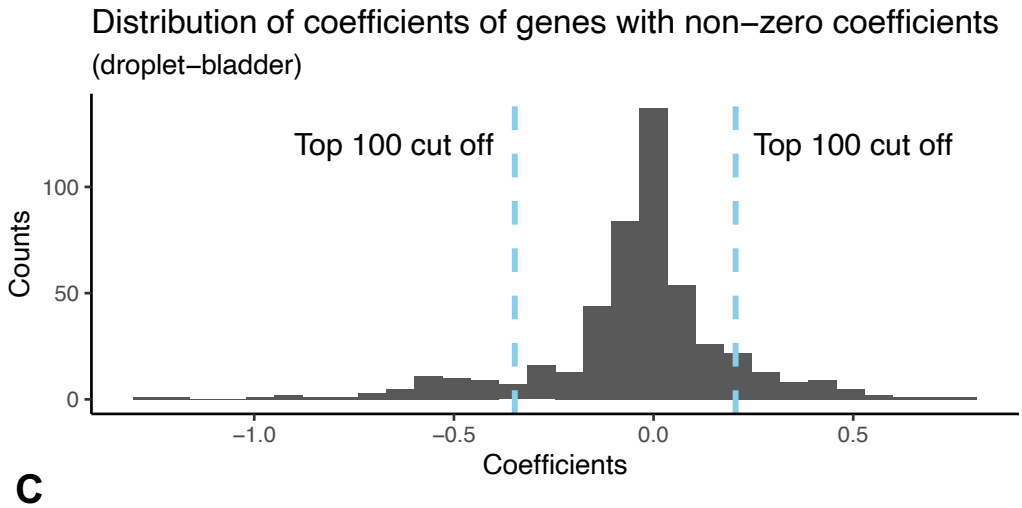

C

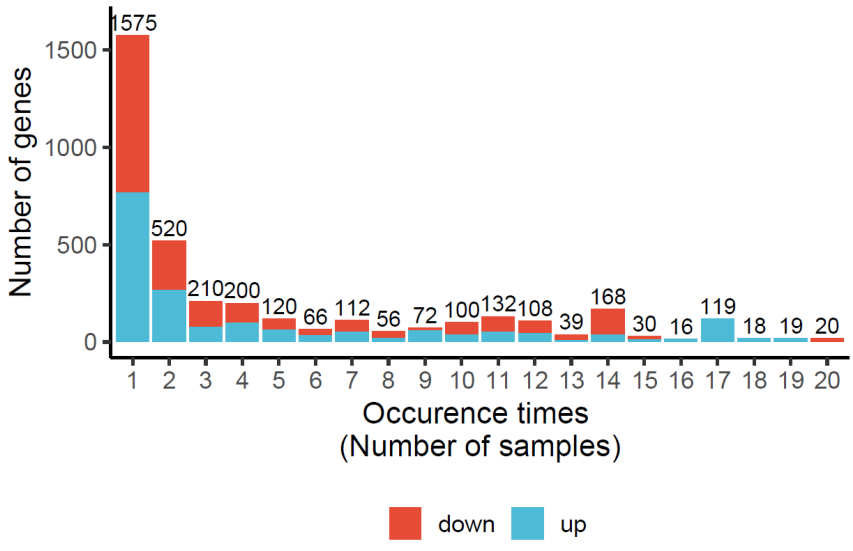

Figure S7. Training SCALE

(A) The overlap between Aging Map and selected aging genes by our forward selection based Elastic-Net method. X-axis shown how many genes we added when performing forward selection.

(B) The plot shows the distribution of non-zero coefficients. The blue dashed lines show the cutoffs of coefficients for the top 100 aging genes.

(C) The overlap among selected genes for each tissue.

Figure S8. Summary of enriched GO terms in aging gene sets across tissues.

A

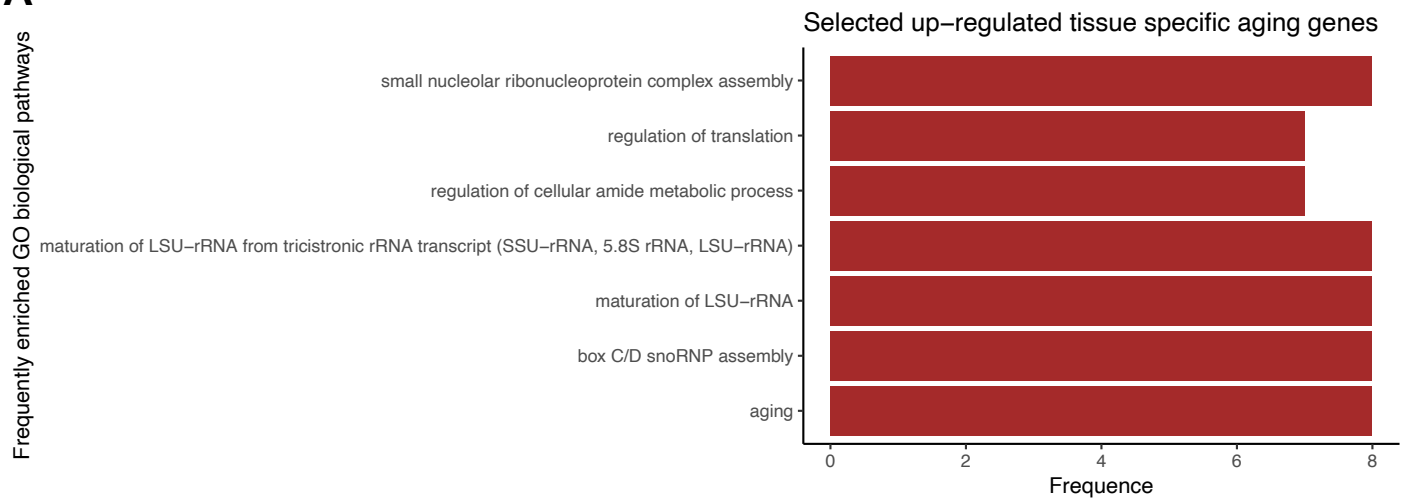

B

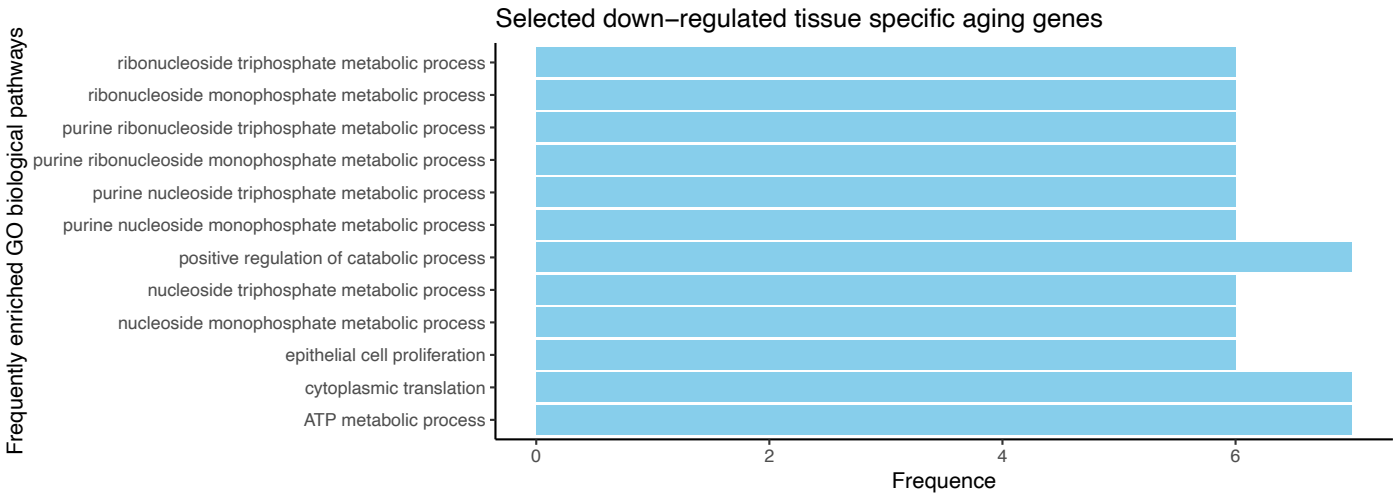

Figure S8. Summary of enriched GO terms in aging gene sets across tissues. For the aging gene sets (up- and down-regulated) selected in each tissue, we performed GO enrichment analysis and recorded enriched GO terms separately. Here the bar plot show the most frequently enriched GO pathways across tissues (A: up-regulated aging genes; B: down-regulated aging genes). X axis shows the number of samples (tissues) where a given GO pathway was enriched in the sample's aging gene set.

Figure S9. Expression level of *Lars2*.

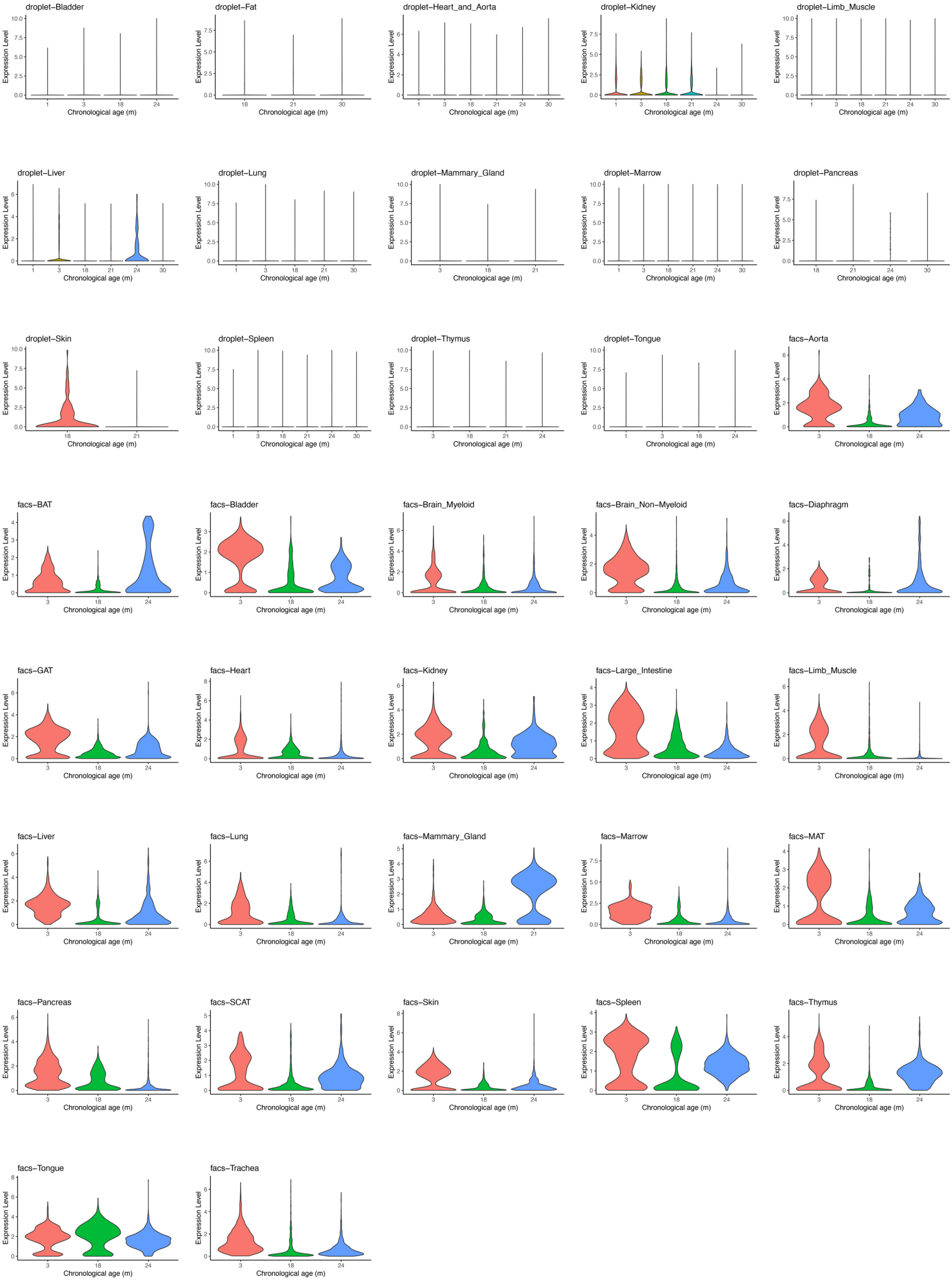

Figure S9. Expression level of *Lars2.*
Violin plots of *Lars2* expression distribution in cells of different tissues and different ages**.**

Figure S10. Expression level of *Rpl13a.*

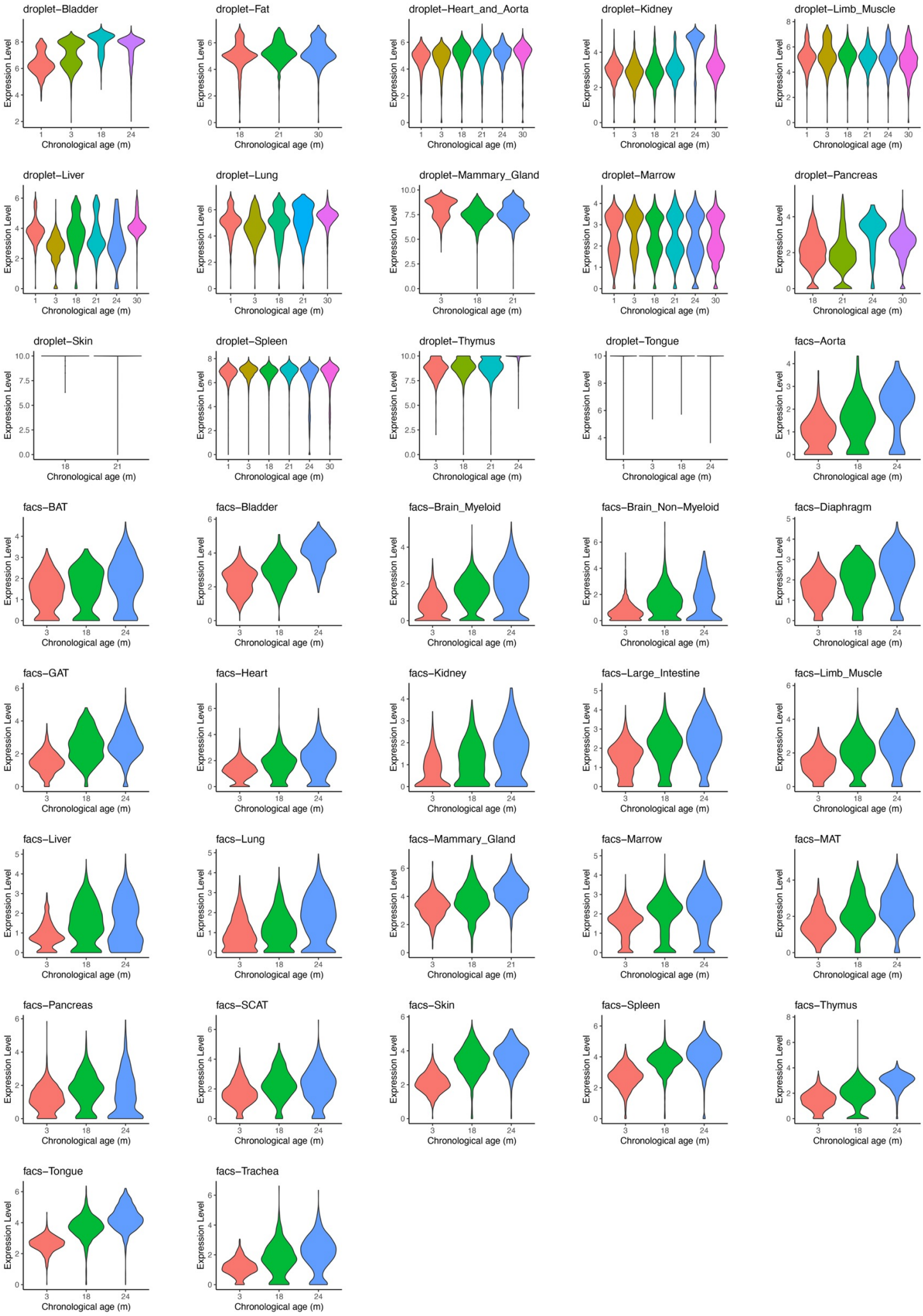

Figure S10. Expression level of *Rpl13a.*
Violin plots of *Rpl13a* expression distribution in cells of different tissues and different ages**.**

Figure S11. SCALE score distributions in different tissues.

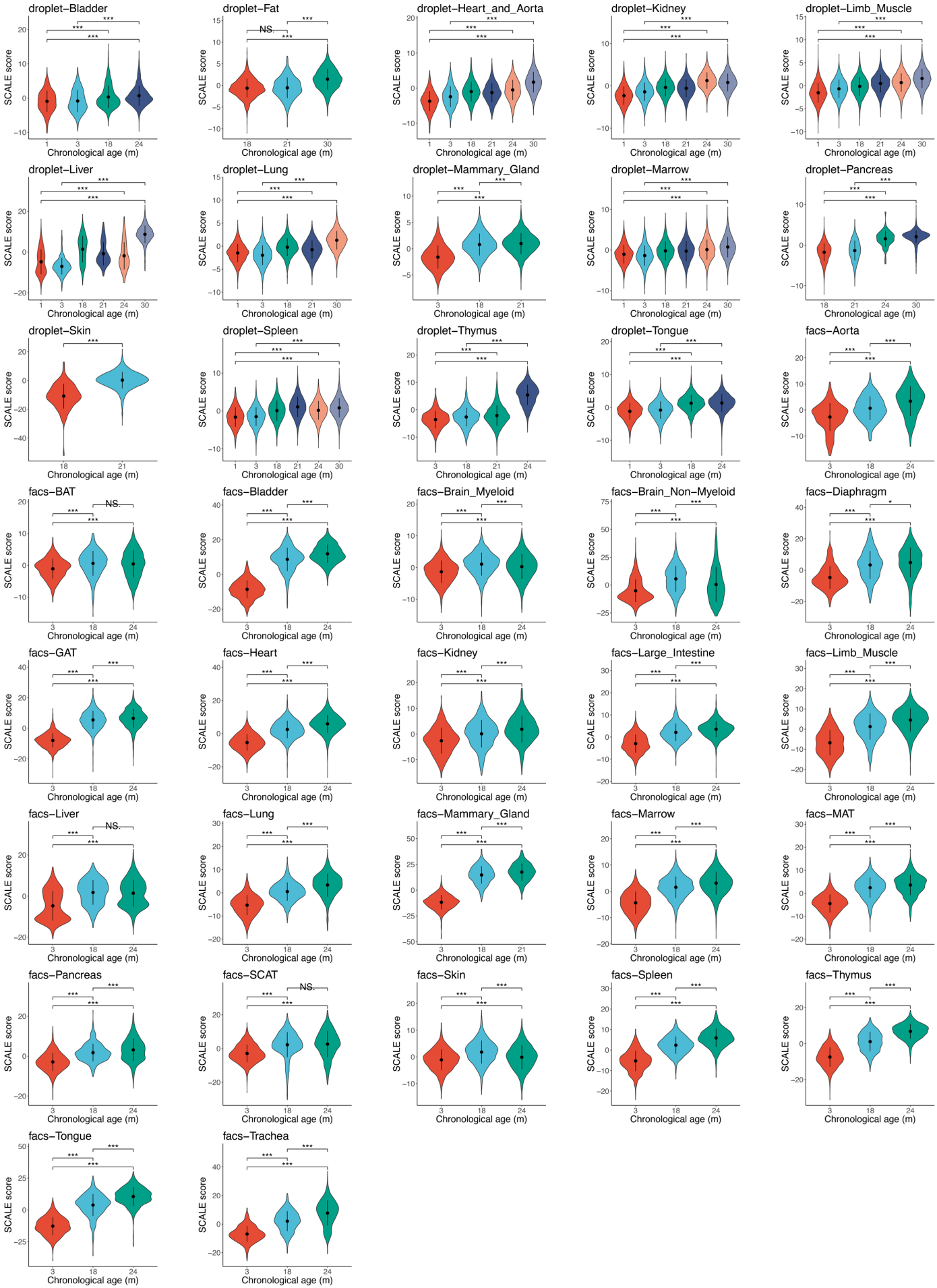

Figure S11. SCALE score distributions in different tissues.
Data are presented as the mean ± s.d. ***p-value < 0.001, **P-value < 0.01 and *P-value < 0.05 using a two-sided unpaired Student's *t*-test.

Figure S12. Robustness of selected aging gene sets.

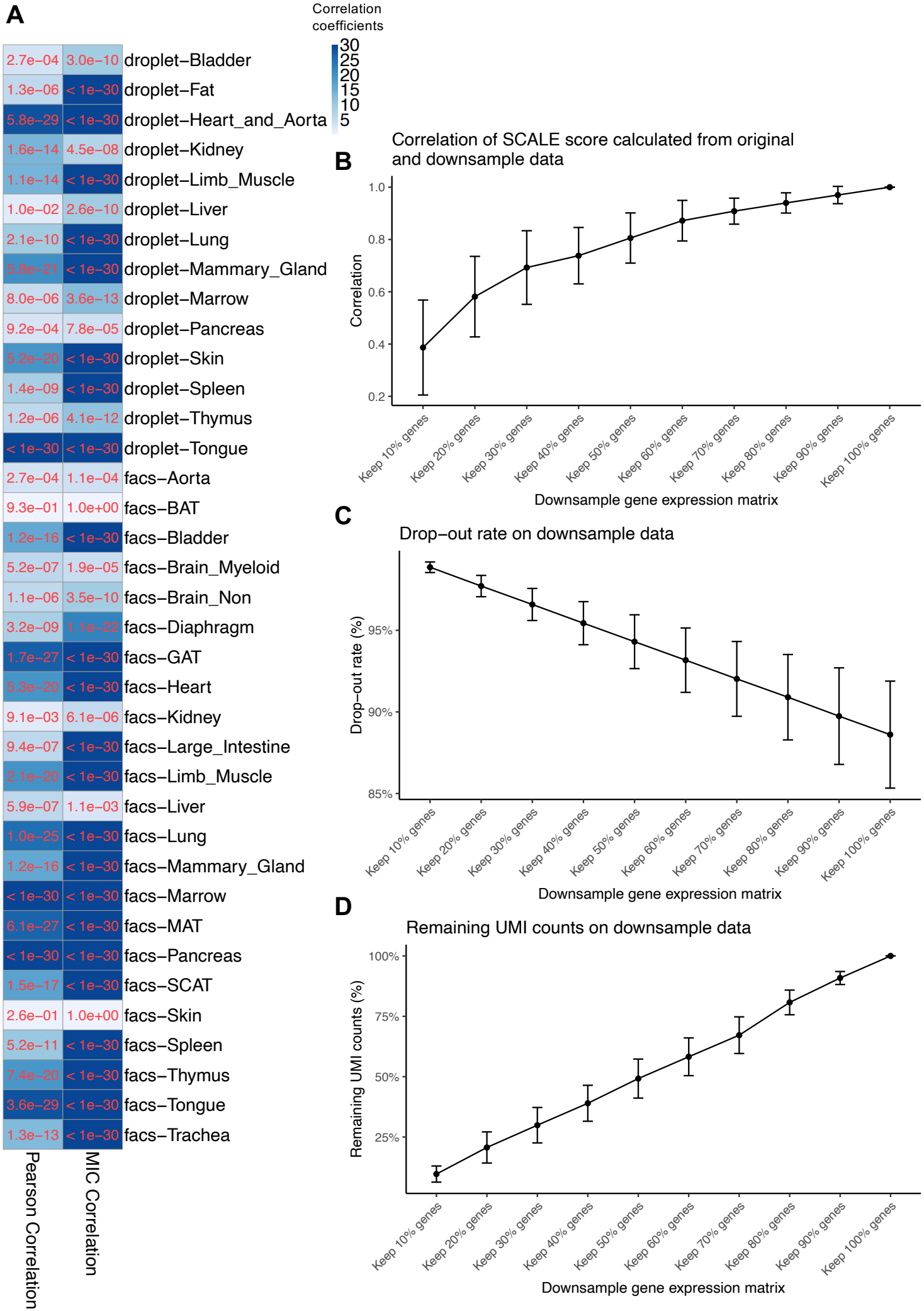

Figure S12. Robustness of selected aging gene sets.
(A) For each tissue, we randomly selected 100 genes from each sample and applied the method used to calculate the SCALE score to compute a score based on these genes. Next, we calculated the Pearson's correlation coefficient between the scores and chronological age to construct the empirical null distribution. Numbers in boxes show adjusted p-value according to the null (corrected by the Benjamini-Hochberg procedure)
(B) Correlation between the SCALE score calculated from original data and data downsampled to different depths (x-axis). Data are presented as the mean ± s.d.
(C) The plot shows the change in the drop-out rate when downsampling the data. The x-axis shows the degree of downsampling. Data are presented as the mean ± s.d.
(D) The plot show the change in the number of remaining UMI counts when downsampling the data. The x-axis shows the degree of downsampling. Data are presented as the mean ± s.d.

Figure S13. Correlations of SCALE scores calculated by different sizes of aging gene sets

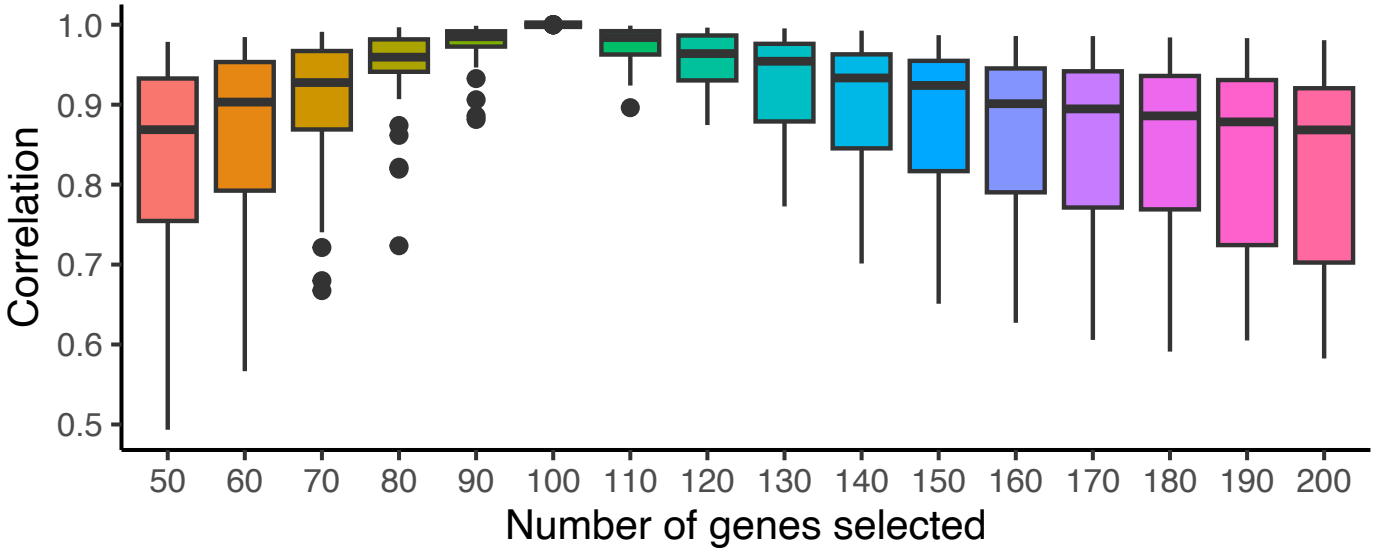

Figure S13. Correlations of SCALE scores calculated by different sizes of aging gene sets

The boxplot shows the correlations of SCALE scores calculated by different sizes of aging gene sets (top 50 genes to top 200 genes) in different tissues.

Figure S14. The mean number of somatic mutations in genes increases during aging across tissues.

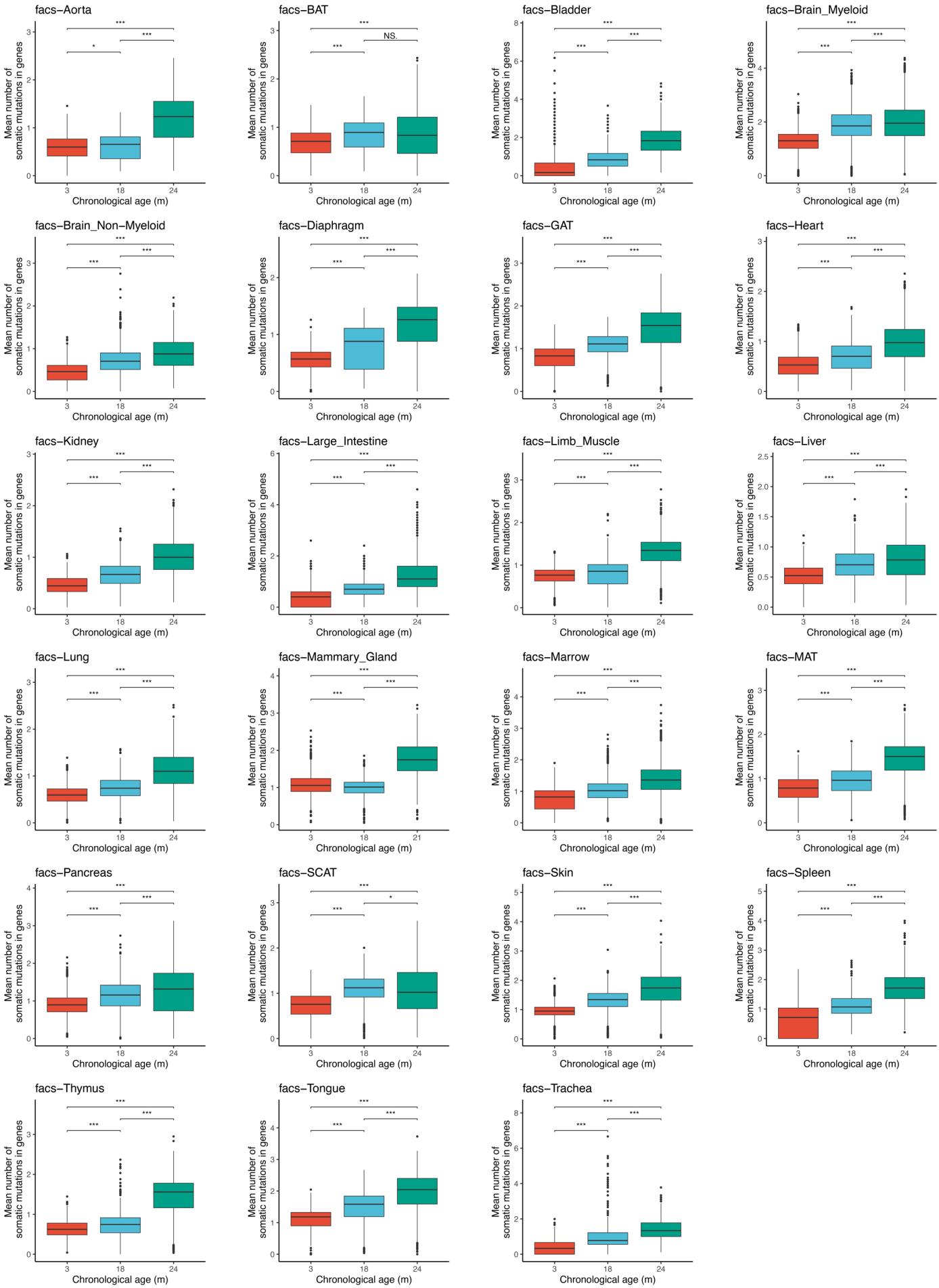

Figure S14. The mean number of somatic mutations in genes increases during aging across tissues.

Standard boxplots showing the distributions of mutation burden (called from single-cell RNA-seq data) of cells in different tissues and age groups.

Figure S15. Relationship between the mean number of somatic mutations in genes and the SCALE score.

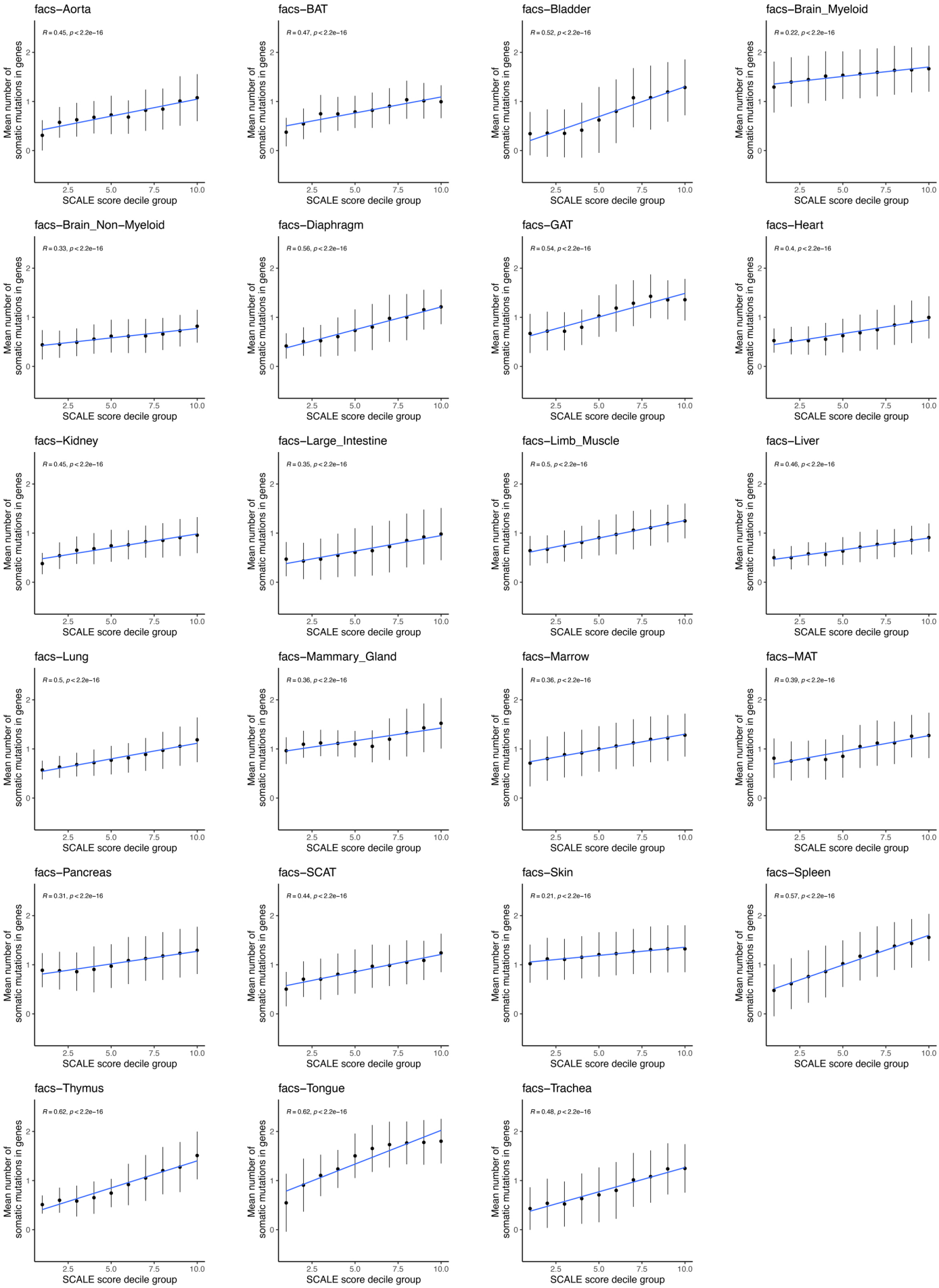

Figure S15. Relationship between the mean number of somatic mutations in genes and the SCALE score.

Blue lines and corresponding annotations represent linear regression models fitted to the mean number of somatic mutations in genes and the SCALE score (divided into 10 groups from low to high). Data are presented as the mean ± s.d.

Figure S16. Relationship between the mean number of somatic mutations in genes and the SCALE score residual.

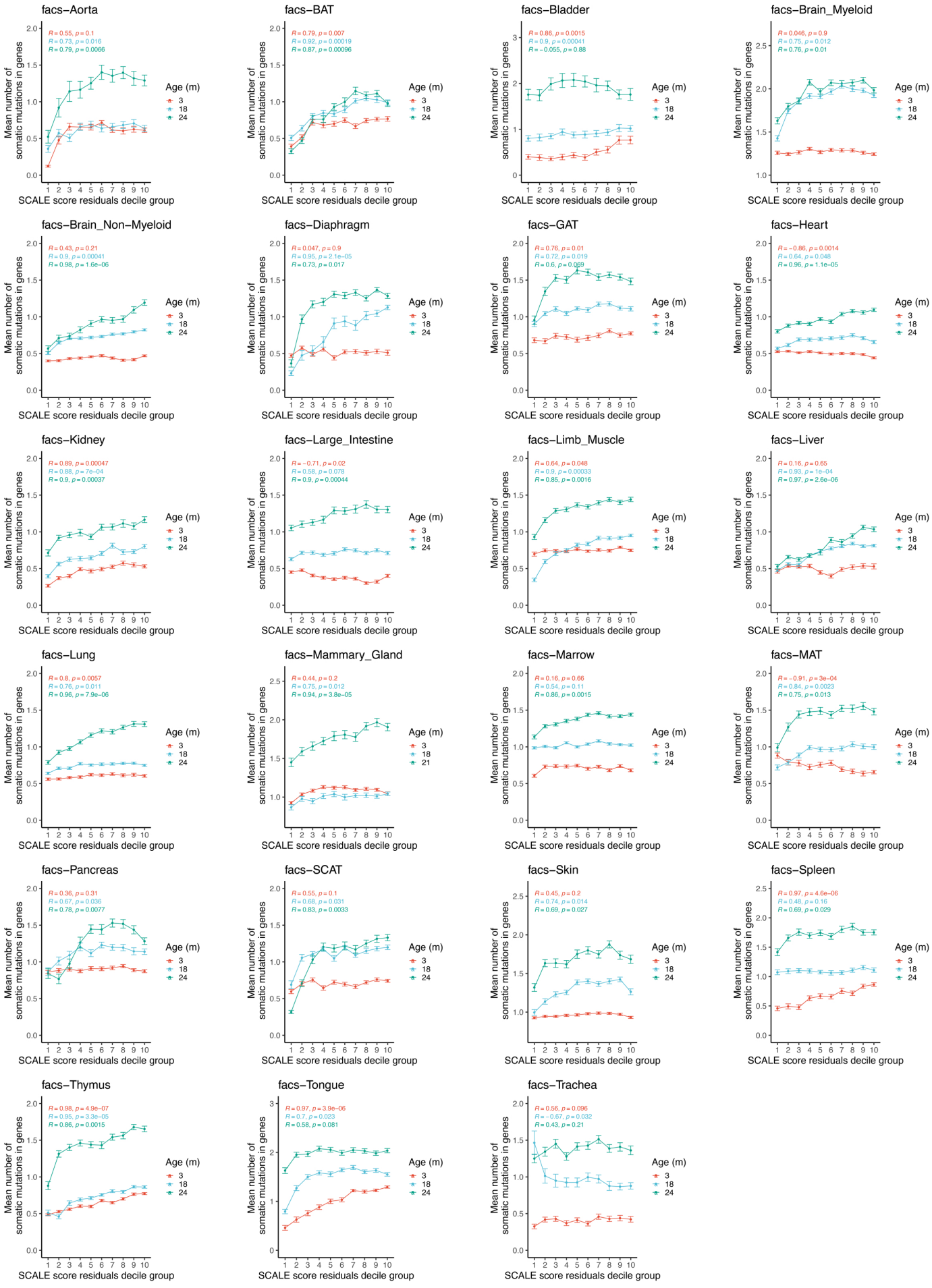

Figure S16. Relationship between the mean number of somatic mutations in genes and the SCALE score residual.
Similar to Figure S15 but here the x-axis in each plot represents SCALE score residuals after regressing out the chronological age.

Figure S17. SCALE outperformed other single-cell clocks in brain Non-microglia cells of mice.

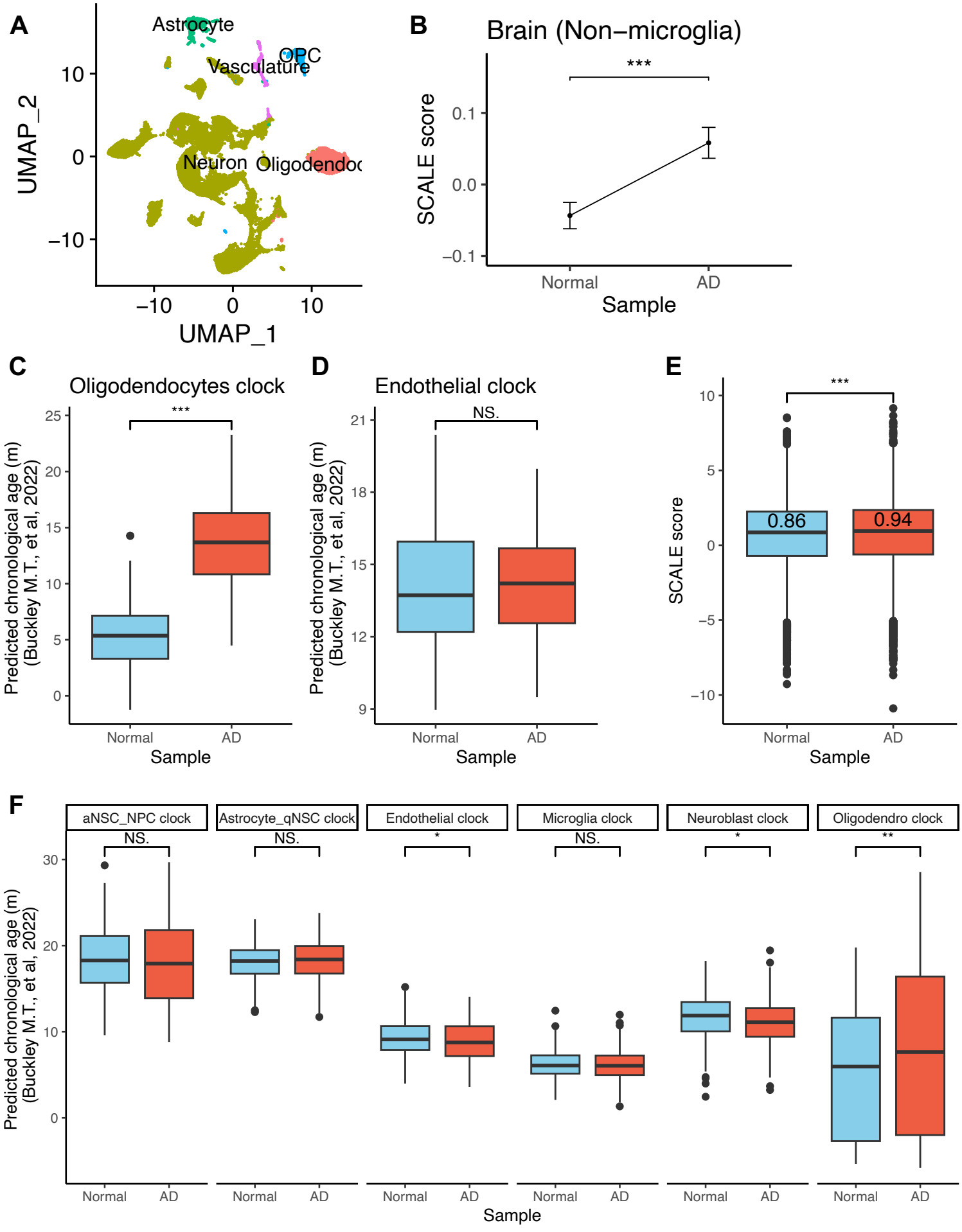

Figure S17. SCALE outperformed other single-cell clocks in brain Non-microglia cells of mice.

(A) Uniform manifold approximation and projection (UMAP) plot brain Non-microglia cells of mice. Different colors show different cell types.

(B) SCALE scores of brain Non-microglia cells from wild type mice (normal, blue) and AD mouse models (AD, red). Data are presented as the mean ± s.e.

(C) Box plot shows predicted chronological age of oligodendrocytes using corresponding clocks reported by Buckley MT, et al.

(D) Box plot shows predicted chronological age of endothelial cells using corresponding clocks reported by Buckley MT, et al.

(E) Predicted chronological age of brain cell types (Neuron, Astrocyte, and OPC) lacking clocks trained by Buckley MT, et al. This box plot shows the results calculated by all six clocks developed by Buckley MT, et al.

(F) SCALE scores of the brain cell types (in the panel E) lacking clocks trained by Buckley MT, et al. The numbers show median values of SCALE scores of cells from wild type mice (normal, blue) and AD mouse models (AD, red).

*p-value < 0.05, **p-value < 0.01, ***p-value < 0.001 using a two-sided unpaired Student's *t*-test.

Figure S18. SCALE scores in different tissues from old mice, young mice, old heterochronic mice and young heterochronic mice

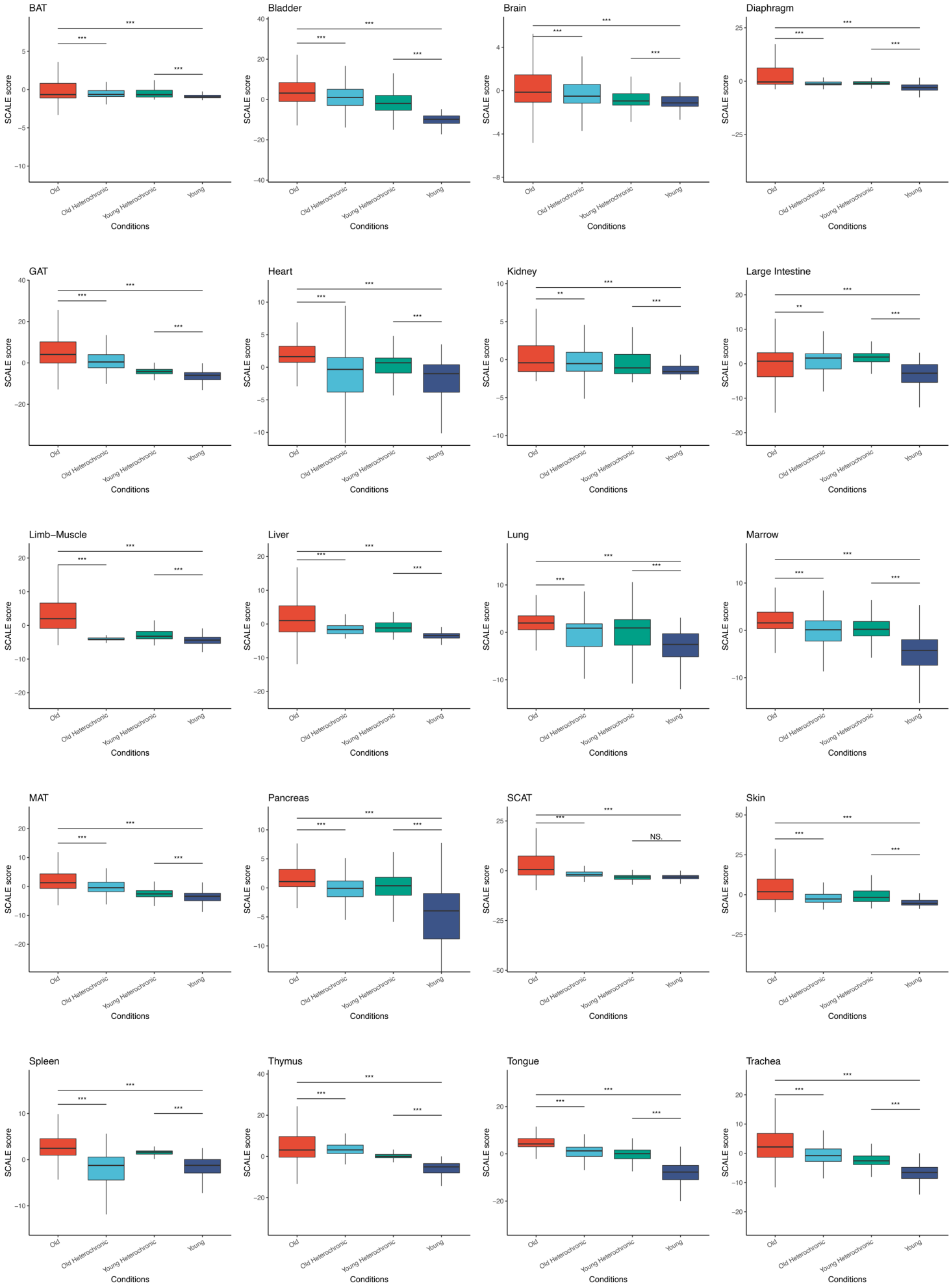

Figure S18. SCALE scores in different tissues from old mice, young mice, old heterochronic mice and young heterochronic mice

SCALE scores of each tissue from old mice, young mice, old heterochronic mice and young heterochronic mice, respectively. **p-value < 0.01 and ***p-value < 0.001 using a two-sided unpaired Student's *t*-test.

Figure S19. Predicted chronological age of different cell types by the method reported by Buckley MT, et al. from old mice, young mice, old heterochronic mice and young heterochronic mice

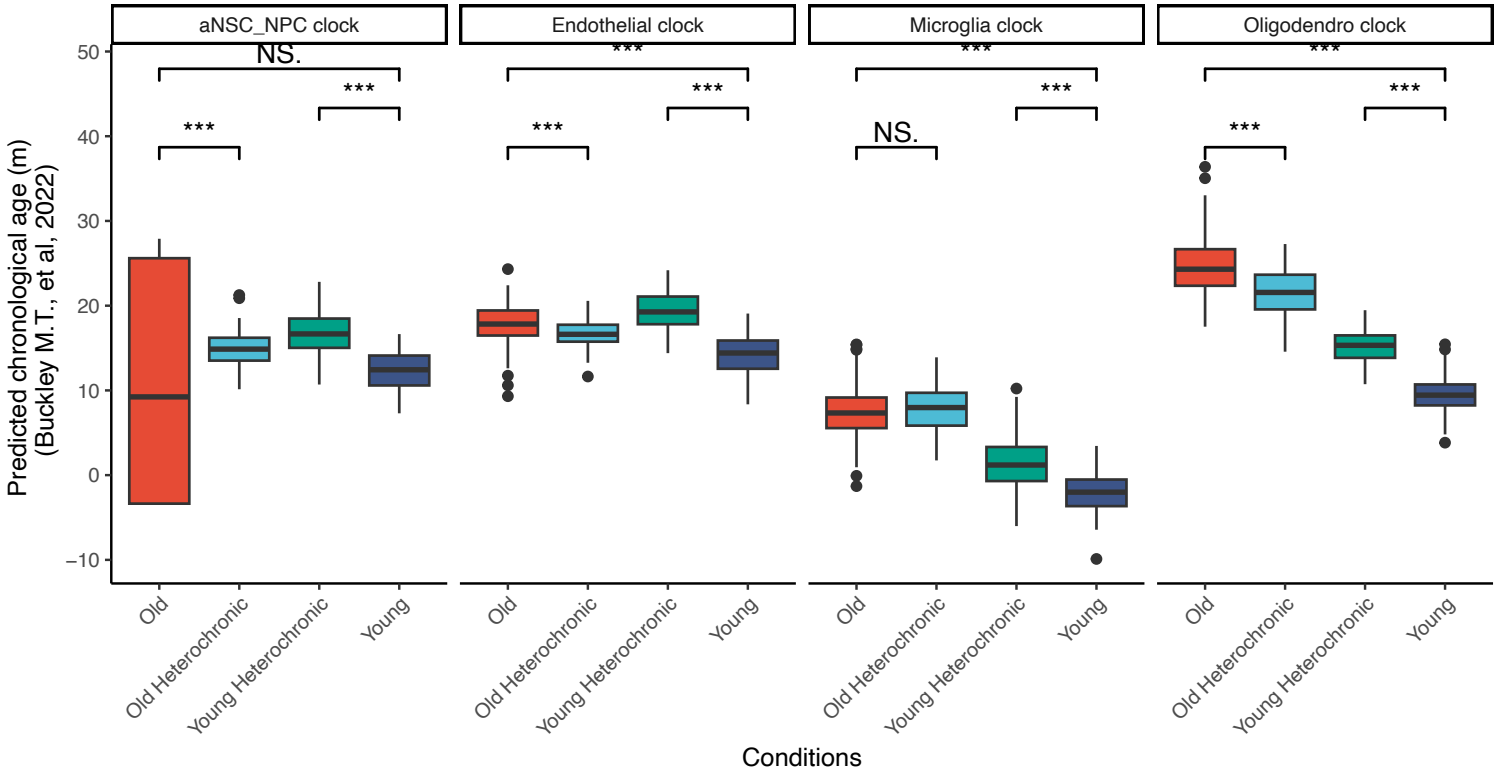

Figure S19. Predicted chronological age of different cell types by the method reported by Buckley MT, et al. from old mice, young mice, old heterochronic mice and young heterochronic mice

Box plots show predicted chronological age of NSCs, endothelial cells, microglia cells, and oligodendocytes cells using corresponding clocks reported by Buckley MT, et al. ***p-value < 0.001 using a two-sided unpaired Student's *t*-test.

Figure S20. Cell-type-specific clocks trained by Buckley MT, et al cannot distinguish parabiosis effects when applied to unseen cell types

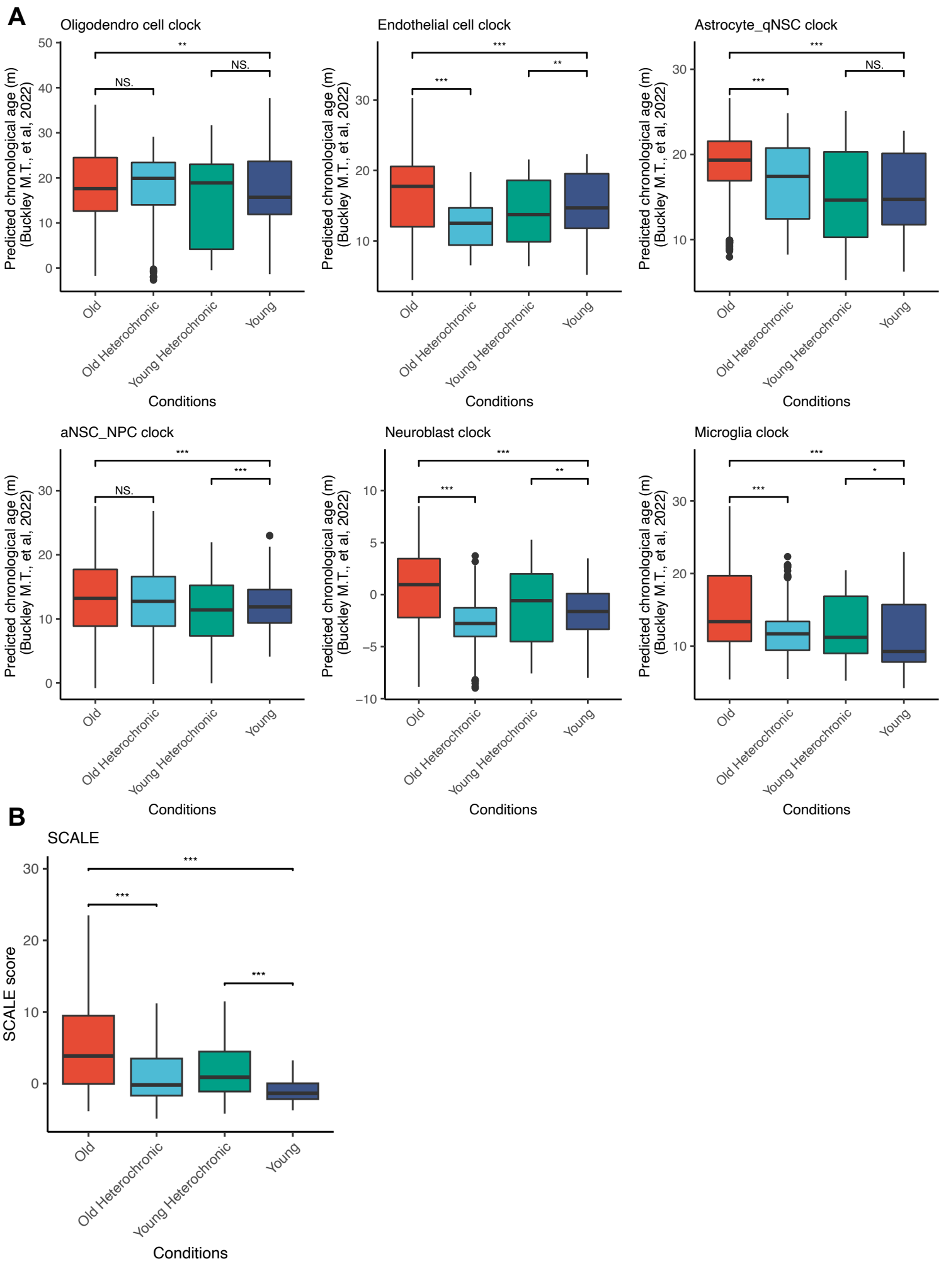

Figure S20. Cell-type-specific clocks trained by Buckley MT, et al cannot distinguish parabiosis effects when applied to unseen cell types

(A) Box plots showing predicted chronological age of brain cell types (ependymal cell, macrophage, neuron, oligo pre cell, pericyte, and T cell) lacking clocks trained by Buckley MT, et al.

(B) Box plot showing SCALE scores of cells from the same cell types in A. *p-value < 0.05, **p-value < 0.01, and ***p-value < 0.001 using a two-sided unpaired Student's *t*-test.

Figure S21. Generalizing SCALE to human data.

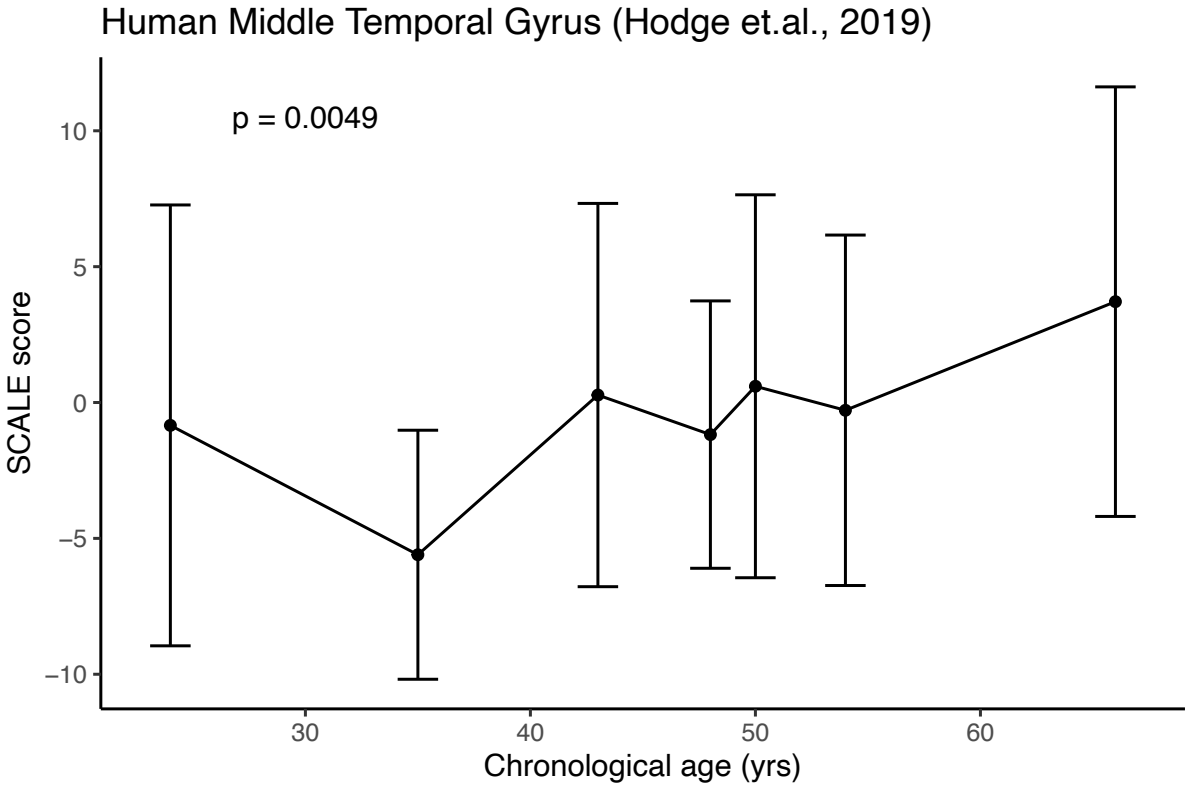

Figure S21. Generalizing SCALE to human data.
We applied mouse-data-trained SCALE on a human middle temporal gyrus dataset. Data are presented as the mean ± s.d. , and the p-value of the linear regression between chronological age and SCALE scores are shown.

Figure S22. Generalizing SCALE to calorie restriction rat data.

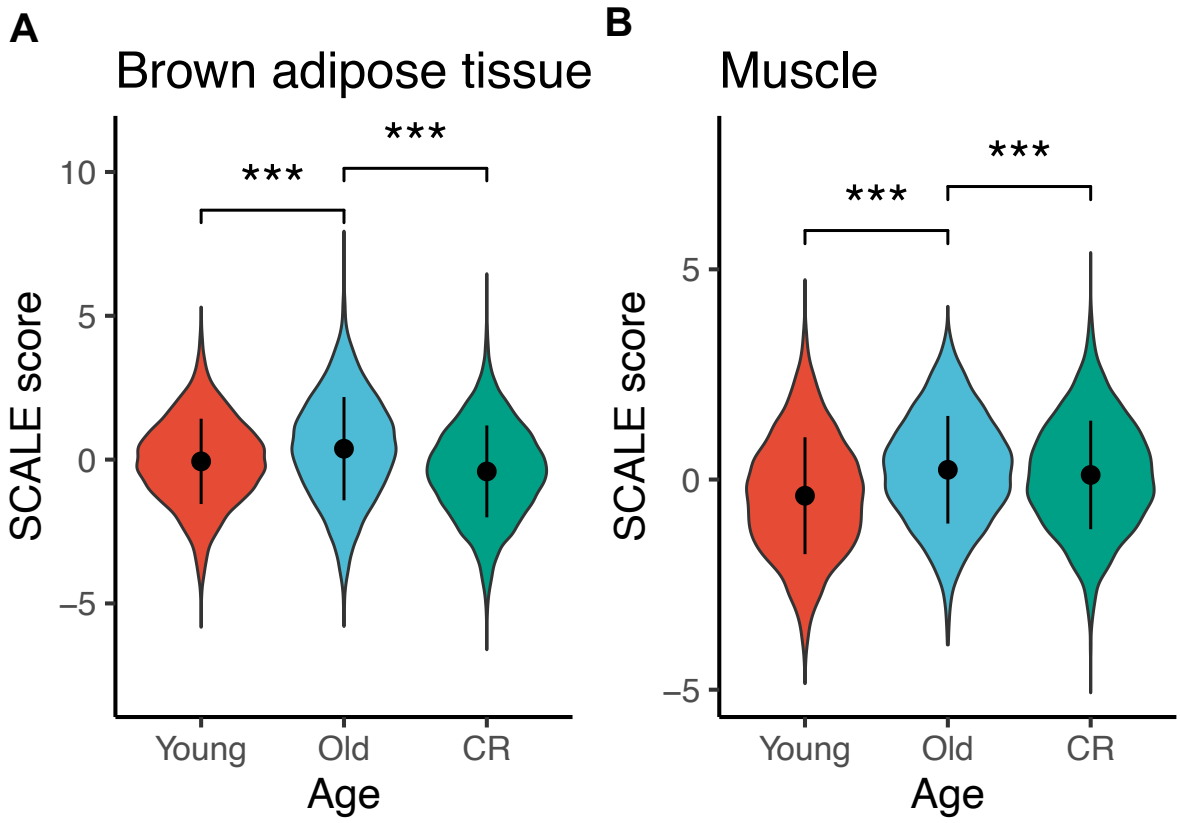

Figure S22. Generalizing SCALE to calorie restriction rat data.
(A) SCALE score of cells in brown adipose tissue of young, old, and calorie restriction rats.
(B) SCALE score of muscle cells of young, old, and calorie restriction rats.
Data are presented as the mean ± s.d. p-values were calculated using two-sided unpaired Student's *t*-tests.

Figure S23. Correlation between SCALE Score and chronological age in different cell types

Figure S23. Correlation between the SCALE score and chronological age for different cell types

Related to Figure 4H. The size of the circle show the Pearson's correlation coefficient. p-values were calculated using a permutation-based test. Orange indicates that the coefficient is significantly larger, and blue indicates that the coefficient is significantly smaller (p-value < 0.05).

Figure S24. Comparison between SCALE and models trained with random initial genes

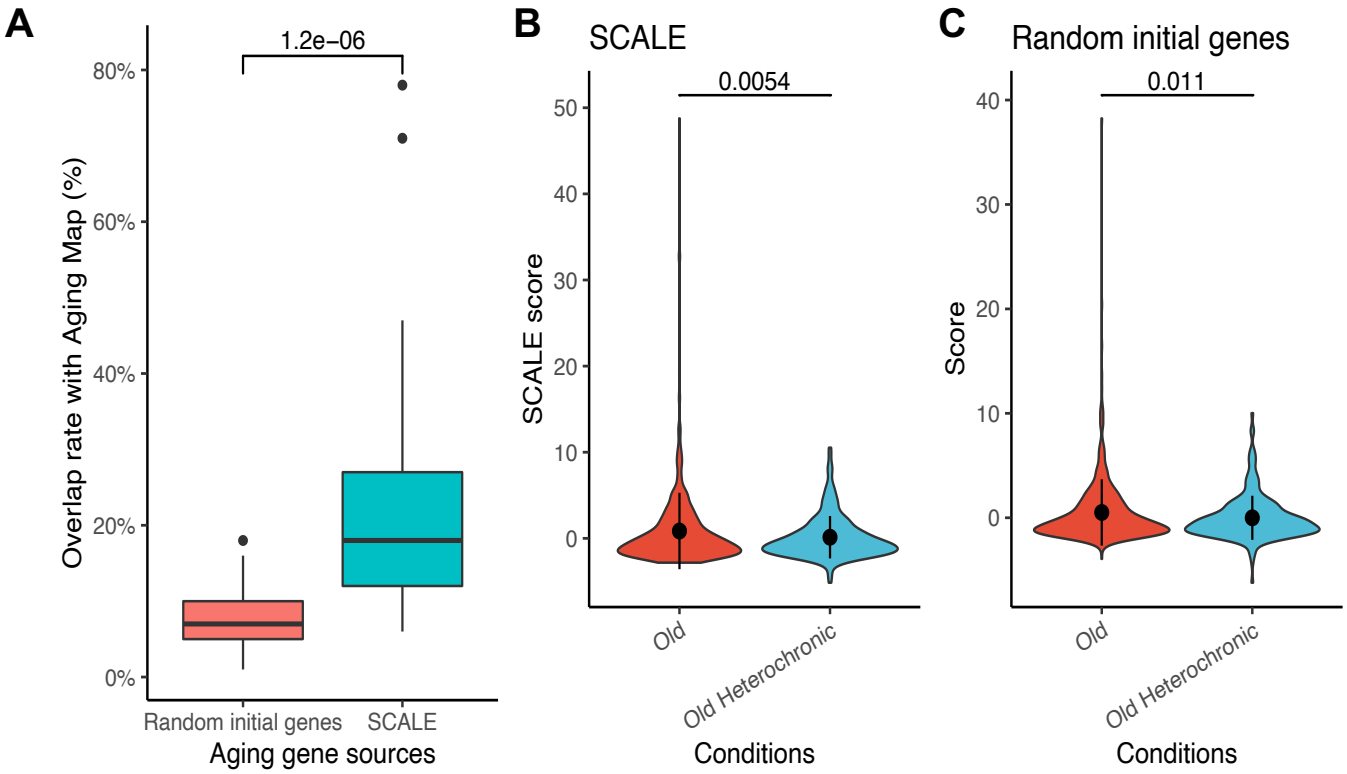

Figure S24. Comparison between SCALE and models trained with random initial genes

(A) Overlap between genes in Aging Map and aging genes selected by random initialization and SCALE's guided forward selection approach. p-values using a two-sided unpaired Student's *t*-test.

(B) SCALE scores of kidney cells from parabiosis mice, calculated using different gene sets. p-values using a two-sided unpaired Student's *t*-test are shown.

(C) SCALE scores of kidney cells from parabiosis mice, calculated using different gene sets. p-values using a two-sided unpaired Student's *t*-test are shown.

Figure S25. Interpolation of SCALE scores using optimal transport.

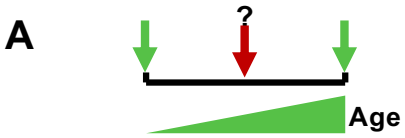

Interpolation in sampling interval

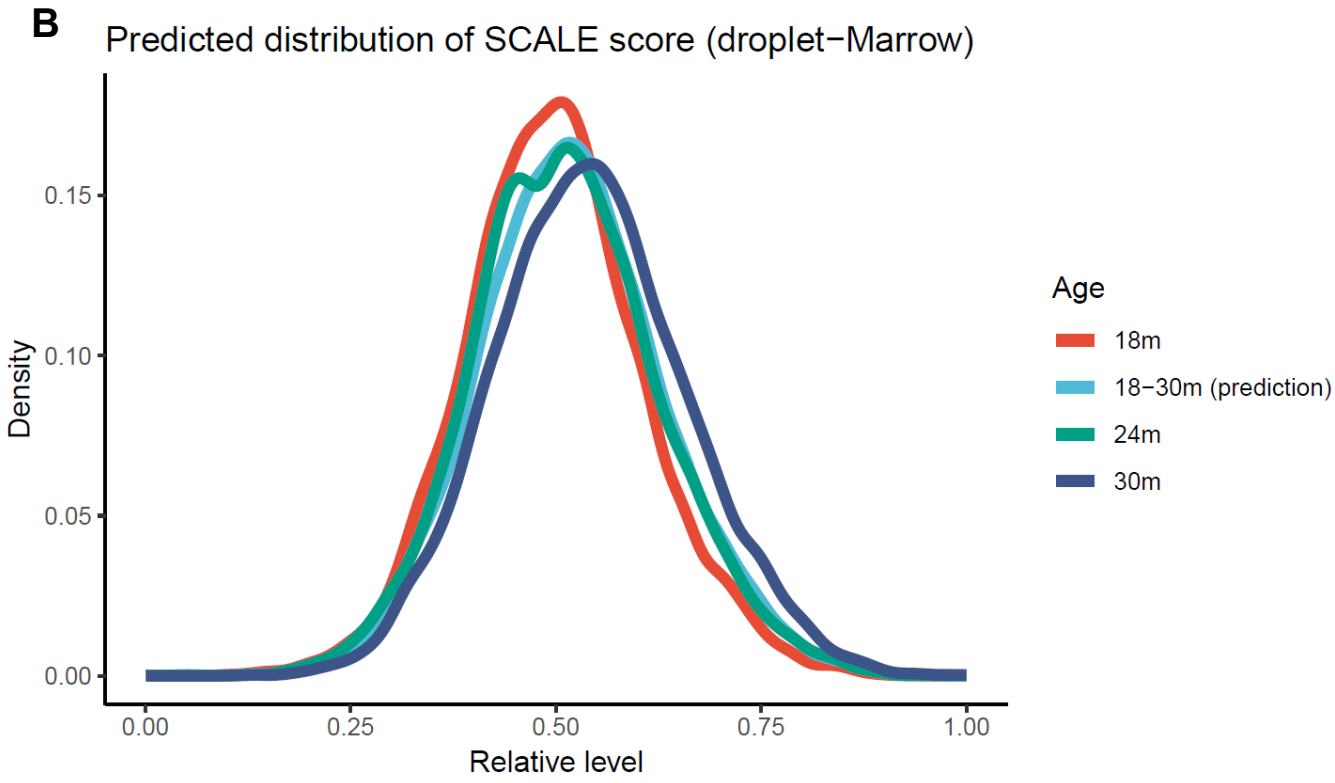

Figure S25. Interpolation of SCALE scores using optimal transport.
(A) Depiction of the interpolation in the sampling interval.
(B) Interpolation of SCALE scores between 18- and 30-month-old groups in marrow. We computed the barycenter of the 18- and 30-month-old groups by optimal transport and compared the distribution to the actually observed 24-month-old group.